journal of the mechanical behavior of biomedical materials 143 (2023) 105941

Contents lists available at ScienceDirect

Journal of the Mechanical Behavior of Biomedical Materials

journal homepage: www.elsevier.com/locate/jmbbm

Load-induced fluid pressurisation in hydrogel systems before and after reinforcement by melt-electrowritten fibrous meshes☆

Eng Kuan Moo [a,b,c,*], Mohammadhossein Ebrahimi [a], Andrei Hrynevich [d], Mylène de Ruijter [d], Miguel Castilho [d,e], Jos Malda [d,f], Rami K. Korhonen [a]

[a] Department of Technical Physics, University of Eastern Finland, Finland
[b] Department of Mechanical and Aerospace Engineering, Carleton University, Canada
[c] Human Performance Laboratory, Faculty of Kinesiology, University of Calgary, Canada
[d] Department of Orthopaedics, University Medical Center Utrecht, the Netherlands
[e] Department of Biomedical Engineering, Eindhoven University of Technology, the Netherlands
[f] Department of Clinical Sciences, Faculty of Veterinary Medicine, Utrecht University, the Netherlands

ARTICLE INFO

Keywords:
Gelatin methacryloyl
Agarose
Alginate
Fluid load support
Micro-indentation
Unconfined compression
Poroelasticity
Viscoelasticity
Reinforced scaffolds

ABSTRACT

Fluid pressure develops transiently within mechanically-loaded, cell-embedding hydrogels, but its magnitude depends on the intrinsic material properties of the hydrogel and cannot be easily altered. The recently developed melt-electrowriting (MEW) technique enables three-dimensional printing of structured fibrous mesh with small fibre diameter (20 μm). The MEW mesh with 20 μm fibre diameter can synergistically increase the instantaneous mechanical stiffness of soft hydrogels. However, the reinforcing mechanism of the MEW meshes is not well understood, and may involve load-induced fluid pressurisation. Here, we examined the reinforcing effect of MEW meshes in three hydrogels: gelatin methacryloyl (GelMA), agarose and alginate, and the role of load-induced fluid pressurisation in the MEW reinforcement. We tested the hydrogels with and without MEW mesh (i.e., hydrogel alone, and MEW-hydrogel composite) using micro-indentation and unconfined compression, and analysed the mechanical data using biphasic Hertz and mixture models. We found that the MEW mesh altered the tension-to-compression modulus ratio differently for hydrogels that are cross-linked differently, which led to a variable change to their load-induced fluid pressurisation. MEW meshes only enhanced the fluid pressurisation for GelMA, but not for agarose or alginate. We speculate that only covalently cross-linked hydrogels (GelMA) can effectively tense the MEW meshes, thereby enhancing the fluid pressure developed during compressive loading. In conclusion, load-induced fluid pressurisation in selected hydrogels was enhanced by MEW fibrous mesh, and may be controlled by MEW mesh of different designs in the future, thereby making fluid pressure a tunable cell growth stimulus for tissue engineering involving mechanical stimulation.

1. Introduction

Hydrogels are hydrophilic polymers that can hold large amounts of water (Lee and Mooney, 2012; Roach et al., 2016; Yue et al., 2015) and are important in cell-based tissue engineering (TE) as they provide three-dimensional (3D) structural support and hydrated environment for cell growth and phenotype maintenance (Benya and Shaffer, 1982). However, hydrogels are mechanically soft and unsuitable for the repair of stiff connective tissues such as cartilage and meniscus. Increasing hydrogel concentration enhances stiffness, but negatively impacts cell growth and phenotype (Bian et al., 2013; Bryant et al., 2004). Although cell-seeded hydrogels cultured *in vitro* can achieve compressive stiffness matching that of connective tissues (Bian et al., 2010), the fabrication process is time- and labour-intensive, and does not fit the clinical off-the-shelf criterion. Various strategies have been developed to create macroscopically stiff hydrogels, while maintaining the local softness of the hydrogel for cell growth. One effective way is by reinforcing the soft hydrogel with a fibrous scaffold, made with an additive manufacturing

☆ *Dedicated to the memory of C. P. Moo (1954–2022).

* Corresponding author. Department of Mechanical and Aerospace Engineering, Carleton University, Canada.
E-mail addresses: EngKuanMoo@cunet.carleton.ca, ekmoo@ucalgary.ca, engkuan.moo@uef.fi (E.K. Moo), mohammadhossein.ebrahimi@uef.fi (M. Ebrahimi), a.hrynevich@umcutrecht.nl (A. Hrynevich), m.deruijter@umcutrecht.nl (M. de Ruijter), m.dias.castilho@tue.nl (M. Castilho), j.malda@umcutrecht.nl (J. Malda), rami.korhonen@uef.fi (R.K. Korhonen).

https://doi.org/10.1016/j.jmbbm.2023.105941
Received 16 February 2023; Received in revised form 25 May 2023; Accepted 28 May 2023
Available online 29 May 2023

technique called melt-electrowriting (MEW) that produces micrometer-sized tension-resistant fibers (Castilho et al., 2018; Visser et al., 2015). The macroscopic stiffness of the MEW mesh-hydrogel composite was greatly enhanced by up to 50 times compared to its constituent parts, a phenomenon that was exclusive to MEW scaffold with fibre diameter <20 μm (Castilho et al., 2018; Visser et al., 2015). The reinforcing mechanism of MEW fibrous meshes is thought to result from a synergistic interaction between the hydrogels and the MEW fibrous scaffold, such that the hydrogel prevents the buckling of the scaffold, thus allowing for effective load transfer through the fibre cross-sectional interconnections (Castilho et al., 2018). The tensing of the tension-resistant MEW fibres during compressive loading effectively restricts the lateral expansion of hydrogels and macroscopically stiffens the MEW-hydrogel composite (Castilho et al., 2018; Visser et al., 2015). Also, the high interfacial shear stresses between the hydrogel and the MEW fibres was thought to prevent the outflow of hydrogel from the fibrous scaffold, thereby resulting in an increase to the overall stiffness of the MEW mesh-hydrogel composite (Visser et al., 2015; Boere et al., 2014). Importantly, the role of fluid pressurisation, which plays a crucial role in enhancing the dynamic mechanical properties of biological tissues such as cartilage (Ateshian, 2009), in the reinforcing mechanism of MEW mesh has never been studied.

In view of the unique reinforcing effect of fibrous mesh with small fibre diameter, MEW meshes have been applied to gelatin methacryloyl (GelMA), norbornene-modified hyaluronic acid (NorHA), and poly (ethylene glycol) (PEG) hydrogels (Castilho et al., 2018; Visser et al., 2015; Bas et al., 2017; Galarraga et al., 2021). Important insights into the reinforcing mechanism of MEW meshes can be gained by applying the MEW meshes in other hydrogel systems that are different in structure and composition, such as agarose and alginate. Unlike GelMA, which is a derivative of a polypeptide (*i.e.,* gelatin), agarose and alginates are linear polysaccharides. Agarose and alginate have been extensively used in TE for their biocompatibility (Lee and Mooney, 2012; Roach et al., 2016). One key difference between these hydrogel systems lies in their cross-linking mechanisms. GelMA hydrogel is a covalently cross-linked hydrogel (Schuurman et al., 2013), while alginate hydrogel can be cross-linked ionically or covalently (Lee and Mooney, 2012). Agarose hydrogels, however, are formed mainly by physical cross-links, such as hydrogen bonds and weak electrostatic interactions through thermal gelation (Roach et al., 2016; Ed-Daoui and Snabre, 2021). The application of MEW meshes on structurally and compositionally different hydrogel systems can be used to provide novel insights into the reinforcing mechanism of the structured fibrous meshes with small fibre diameter.

The cells adjust their phenotype and metabolic activities based on the surrounding mechanical microenvironment (Benya and Shaffer, 1982) which, in the case of hydrogels, is typically measured in terms of instantaneous and equilibrium elastic moduli (Castilho et al., 2018; Visser et al., 2015; Bartnikowski et al., 2015). Mechanical parameter like load-induced fluid pressurisation is often deemed irrelevant and neglected for studies using free-swelling culture conditions, but becomes highly important for various tissue engineering studies involving mechanical stimulation (Bian et al., 2010; Huang et al., 2012; Kock et al., 2013; Mauck et al., 2000). Fluid pressures spanning across three orders of magnitude (from kilo to mega Pascals) have been used as mechanical stimulus for cell growth (Elder and Athanasiou, 2009; Gavénis et al., 2007; Luo and Seedhom, 2007; Miyanishi et al., 2006). However, controlling fluid pressure as a sole mechanical stimulus is not straightforward and typically involves complex experimental set-up (Elder and Athanasiou, 2009). The possibility that MEW fibrous mesh reinforces hydrogels through load-induced fluid pressurisation is exciting as it may offer an alternative to the current methods used to control fluid pressure. However, the mechanism governing the time-dependent mechanical behaviours of the hydrogels can influence the evaluation of the load-induced fluid pressure. Viscoelasticity and poroelasticity are two plausible mechanisms for the time-dependent properties of the hydrogels (Ed-Daoui and Snabre, 2021). Viscoelasticy is caused by molecular re-arrangement and is therefore independent of the fluid flow and the length scale (Fung et al., 2017; Mak, 1986; Nia et al., 2011); whereas poroelasticity is caused by fluid flow through porous media and depends on the fluid flow path length (Nia et al., 2011; Wahlquist et al., 2017). While the time-dependent properties of hydrogels are well predicted by theoretical models assuming either viscoelasticity or poroelasticity (Gu et al., 2003; Hu et al., 2010; Meloni et al., 2017; Miri et al., 2018; Nam et al., 2016; Soltz et al., 1999), identification of the dominant deformation mechanism can help determine the fluid pressure development in the hydrogels, and facilitate the optimal hydrogel design for the control of cell mechanotransduction and metabolism.

Therefore, the current study was aimed at investigating the mechanical properties of different hydrogel systems and the mechanical changes brought upon by the incorporation of gridded MEW meshes in these hydrogels, with emphasis placed on the load-induced fluid pressurisation. We tested three commonly used hydrogel systems that included GelMA, agarose and alginate using micro-indentation and unconfined compression. The material properties were extracted by fitting the mechanical data to an analytical model and a Finite Element model. Specifically, the objectives of this study were five-fold, stated as (i) to determine if MEW meshes enhance the mechanical properties of the hydrogels through fluid pressurisation, and if the same reinforcing mechanism applies equally to all three hydrogel systems, (ii) to study if the grid structure of MEW meshes introduce localised, heterogeneous mechanical reinforcement to the hydrogels, (iii) to determine if viscoelasticity or poroelasticity dominates for different hydrogel systems with and without the MEW meshes, (iv) to investigate if material properties derived by micro-indentation agree with those obtained by unconfined compression, and (v) to evaluate the repeatability of the FE-driven numerical optimisation procedures in determining multi-parametric material properties. Correspondingly, we hypothesised that (i) MEW meshes improve the fluid pressurisation in GelMA, agarose and alginate hydrogels by the same reinforcing mechanism, (ii) MEW meshes only stiffen regional hydrogel that was close to the mesh, but not regions distant from the mesh, (iii) poroelasticity dominates the time-dependent properties of all hydrogels, (iv) mechanical properties derived by micro-indentation test agree with those obtained by unconfined compression, (v) multi-parametric material properties predicted by the numerical optimisation procedure show little variation over repeated runs.

2. Methods

2.1. Sample preparation

2.1.1. Hydrogels

5 mm-diameter hydrogels with a thickness, *h*, of 2 mm were fabricated in a custom-built Teflon mold containing interconnected, matched-sized cylindrical wells. The top and bottom surfaces of the mold were covered by a glass plate.

2.1.1.1. Agarose. Agarose with low gelling temperature (A4018, Sigma Aldrich, St. Louis, MO, USA) was dissolved in phosphate buffered saline (PBS) solution by heating and magnetic stirring to a final concentration of 4% w/v. The agarose solution was injected into the cylindrical well of the mold and cross-linked by cooling to room temperature.

2.1.1.2. Alginate. Sodium alginate (W201502, Sigma Aldrich, St. Louis, MO, USA) was dissolved in distilled water by magnetic stirring for >3 h at a concentration of 4% w/v. The alginate solution was injected into the cylindrical well of the mold, and cross-linked between a sandwich of parallel glass plates wrapped by filter papers that were soaked by 100 mM $CaCl_2$ solution.

2.1.1.3. GelMA. GelMA was synthesised by a reaction of type A gelatin

(G2625, Sigma Aldrich, USA) with methacrylic anhydride at 50 °C for 1 h, as described previously (Van Den Bulcke et al., 2000). 15% (w/v) GelMA solution was prepared by dissolving the freeze-dried GelMA in PBS solution at 37 °C. The GelMA solution was supplemented with 1 mg/ml photoinitiator of lithium phenyl-2,4,6-trimethylbenzoylphosphinate (LAP), before being injected into the cylindrical well of the Teflon mold and photo-crosslinked by ultraviolet light at a wavelength of 405 nm for 20 min.

2.1.2. MEW fibrous meshes

Poly-ε-caprolactone (PCL) fibres were direct-written onto uncoated microscope slides (Menzel, Germany) using a commercial bioprinter with melt-electro writing head (3D Discovery Evolution, regenHU, Switzerland) (de Ruijter et al., 2018; Peiffer et al., 2020). Medical grade PCL pellets (PURAC PC12, Corbion, Netherlands) were melted in a stainless steel syringe by an electrical heating element at 80 °C and extruded vertically at 1 bar through a metal flat-tipped nozzle (24 G, Unimed, Switzerland) onto a glass collector plate underneath. The extruded PCL jet was stabilised by an electric field of 1.5 kV/mm established between the nozzle tip and the collector plate (5 mm apart) and deposited onto the collector plate that was translating horizontally at a speed of 10 mm/s. The PCL fibres of 20 μm diameter were printed in grid structure (inter-fibre spacing: 600 μm) over an area of 4 cm × 4 cm on a layer-by-layer manner for 150 layers, which amounted to a thickness of 2 ± 0.1 mm.

2.1.3. Fibre-reinforced hydrogels

Cylindrical-shaped MEW meshes of 5 mm diameter were cut out by a biopsy punch (Razormed Inc., India) of matched diameter, and placed in the well of the Teflon mold. The hydrogel solutions were then injected into the cylindrical well and allowed to fully perfuse the MEW meshes before being crosslinked, either by cooling (for agarose), by exposure to 100 mM of $CaCl_2$ solution (for alginate), or by exposure to ultraviolet light at 405 nm (for GelMA).

2.1.4. Sample size

For each hydrogel system (GelMA, agarose or alginate), seven replicates of hydrogels without MEW meshes (i.e., non-fibre-reinforced, nonfr) and six replicates of hydrogels with MEW meshes (i.e., fibre-reinforced, fr) were fabricated and underwent mechanical testing.

2.2. Mechanical testing protocols

The protocol used for mechanical testing is illustrated in Fig. 1. All mechanical tests were conducted at room temperature with the crosslinked hydrogels immersed in bathing solution (PBS for GelMA and agarose, distilled water for alginate). The fabrication and mechanical testing of all samples were conducted within 24 h to minimize the impact of potential degradation of the hydrogel.

2.2.1. Indentation

The hydrogels that resided in the Teflon well and sat on a stainless-steel plate were indented by a ruby spherical indenter attached to a

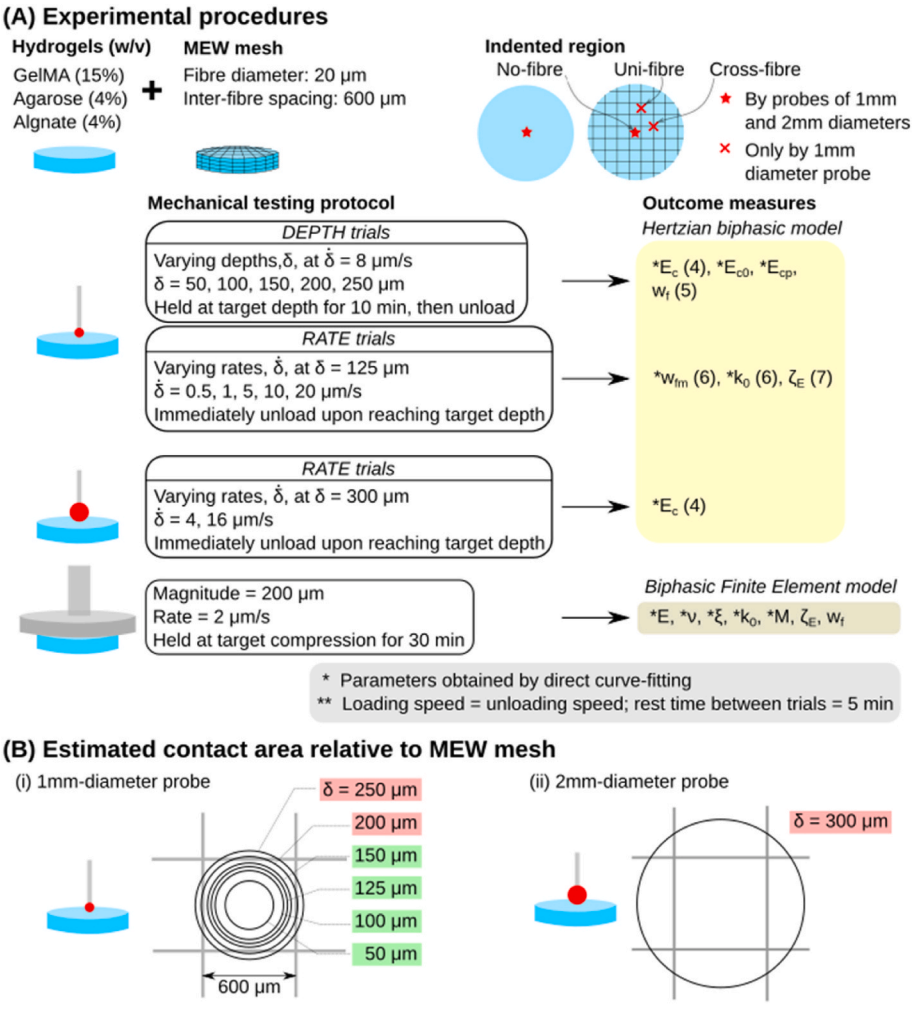

Fig. 1. (A) Graphical illustration of the protocols of mechanical indentation and unconfined compression tests applied to three types of hydrogels (GelMA, agarose and alginate) with and without reinforcement by the MEW meshes. Multiple regions including no-fibre, uni-fibre and cross-fibre regions were indented by spherical indenters of 1 mm and 2 mm diameters. The outcome measures include material parameters that were curve-fitted to a Hertzian biphasic model using indentation data, and to a biphasic fibre-reinforced FE model using unconfined compression data (*i.e.*, those marked by *). The remaining material parameters (*i.e.*, those not marked by *) were subsequently derived from the optimised material model. The mathematical equations associated with the parameters are also indicated in the bracket. (B) The estimated contact area resulting from the varying indentation depths relative to the MEW mesh for indentation over no-fibre region. Contact area which is bound by a unit grid of the MEW mesh (600 × 600 μm^2) is highlighted in green, whereas contact area that goes beyond a unit grid is marked as red.

mechanical tester (Mach-1 v500css, Biomomentum Inc., Laval, Quebec, Canada) equipped with a single axis load cell (MA 999, range: ±150 g, resolution: 75 μN). The indenter was lowered vertically by the mechanical tester towards the hydrogel until contact was established, which was defined as the instant at which the reaction force increased by twice the resolution of the load cell.

1 mm-diameter indenter was used to indent the hydrogels at a fixed loading rate, $\dot{\delta}$, of 8 μm/s to six target depths, δ, ranging from 50 to 250 μm (2.5–12.5% nominal strain) at an increment of 50 μm (Bonnevie et al., 2012). The hydrogels were allowed to stress-relax for 10 min, before being unloaded (denoted as DEPTH trials, Fig. 1). The hydrogels were also indented to a fixed depth of 125 μm at five loading rates, $\dot{\delta}$, of 0.5, 1, 5, 10, and 20 μm/s, and immediately unloaded upon reaching the target depth (indicated as RATE trials, Fig. 1). A rest period of 5 min in between trials was given to allow for material recovery. The indentations were conducted in an order of increasing depth to minimize the effect of potential unrecovered indented volume from prior indentation, except for depths of 150 μm and 200 μm. The indentation order for 150 μm and 200 μm depths was reversed to determine the significance of the order effect. For the nonfr-hydrogels, the 1 mm-indentation protocol was conducted in the middle of the construct; whereas for the fr-hydrogels, the 1 mm-indentation protocol was repeated thrice at regions containing either no MEW fibre (no-fibre), uni-directional MEW fibre (uni-fibre), or crossed MEW fibres (cross-fibre) to evaluate the potential mechanical inhomogeneity caused by the grid structure of the MEW meshes (Fig. 1A). The placement of the indenter was assisted by a camera mapping of the hydrogel surface.

Following the 1 mm-indentation protocol, the indenter was replaced by a 2 mm-diameter indenter. The hydrogels were indented to a target depth of 300 μm at loading rates of 4 and 16 μm/s and immediately unloaded upon arriving at the target depth.

2.2.2. Unconfined compression

The hydrogels were removed from the Teflon well. The indenter was replaced by a compression platen of 12.5 mm diameter. Following the establishment of contact, the hydrogels were compressed without lateral confinement at a loading rate of 2 μm/s to a target depth of 200 μm (10% nominal strain), and stress-relaxed for 30 min.

2.3. Data analysis

Mechanical data from indentation tests were fitted to an analytical biphasic-Hertzian model (Bonnevie et al., 2012; Moore et al., 2015). The data from unconfined compression tests were fitted to a fibre-reinforced biphasic mixture model using a numerical optimisation procedure (Maas et al., 2012).

2.3.1. Curve-fitting of indentation data to a biphasic Hertzian model

The analytical model considers a thin layer of hydrogel samples (h = 2 mm) sitting on a rigid substrate. The top and bottom surfaces of the hydrogel specimen are assumed to be perfectly flat with zero curvature. The Hertzian contact modulus, E_c, measured by a rigid spherical indenter of radius, r, at an indentation depth, δ, is expressed in alternative forms as (Bonnevie et al., 2012; Moore et al., 2015)

$$E_c = \frac{E}{1-\nu^2} \quad \text{Eq. (1a)}$$

$$= \frac{f_c}{\sqrt{r\delta^3}} \quad \text{Eq. (1b)}$$

$$= \frac{3}{4}\frac{f_c}{\delta a} \quad \text{Eq. (1c)}$$

where E and ν are the Young's modulus and Poisson's ratio, respectively,

f_c is the contact force, and

a is the contact radius, defined as $a = \sqrt{r\delta}$.

The contact force was corrected for the substrate effect that artificially stiffens the thin hydrogel layer (Hayes et al., 1972). To that end, the measured force data, F, was multiplied by a factor, f_p, which is a function of the dimensionless layer thickness, $\bar{h} = \frac{h}{a}$, and defined as (Moore et al., 2015; Hayes et al., 1972; Chen and Engel, 1972; Stevanovic et al., 2000):

$$f_p = \left(1 - 1.04\exp\left(-1.73\bar{h}^{0.734}\right)\right)^3 \quad \text{Eq. (2)}$$

The contact force is therefore

$$f_c = f_p F \quad \text{Eq. (3)}$$

By rearranging Eq (1b),

$$f_c = \frac{4}{3}E_c\sqrt{r(\delta-\delta_0)^3} \quad \text{Eq. (4)}$$

where δ_0 represents the offset depth of a few micrometer above the 'true' surface of the analytical model (Moore et al., 2015).

The effective contact modulus, E_c, was obtained from the slope of the linear approximation of f_c vs. $\sqrt{r(\delta-\delta_0)^3}$ curve plotted over the loading phase of the indentation, according to Eq. (4). For DEPTH trials that involved indentation of hydrogels to different depths at a fixed loading rate, the peak (E_{cp}) and near-equilibrium (E_{c0}) contact moduli were calculated using the same procedure that is used for the calculation of E_c, with the exception that the f_c was replaced by either the peak (f_{cp}) or the near-equilibrium (f_{c0}) contact forces, and the δ's (and the corresponding δ_0's) were substituted by the five tested indentation depths (Fig. 1A).

The stress relaxation in the DEPTH trials allows for the measurement of the fluid load fraction, w_f, which is defined as the proportion of load carried transiently by the fluid phase of the hydrogel, and can be estimated from the peak and near-equilibrium contact force or modulus as:

$$w_f = \frac{f_{cp} - f_{c0}}{f_{cp}} \quad \text{Eq. (5a)}$$

$$w_f = \frac{E_{cp} - E_{c0}}{E_{cp}} \quad \text{Eq. (5b)}$$

As the loading rate increases, the fluid load fraction increases proportionally until it plateaus at a maximum fluid load fraction, w_{fm}. The fluid load fraction, w_f, is related to the loading rate, $\dot{\delta}$, by (Bonnevie et al., 2012; Cohen et al., 1998):

$$w_f = w_{fm}\frac{\dot{\delta}r}{\dot{\delta}r + 2E_{c0}k_0} \quad \text{Eq. (6)}$$

where k_0 is the hydraulic permeability with unit of $\mathrm{mm^4N^{-1}s^{-1}}$.

The data obtained from the RATE trials, which indented hydrogels to a fixed depth at different loading rates, were used to fit to Eq (6) for w_{fm} and k by least-squares minimisation through the 'curve_fit' function of a SciPy module (Virtanen et al., 2020). The maximum fluid load fraction was then used to calculate the tension-to-compression modulus ratio (Bonnevie et al., 2012)

$$\zeta_E = \frac{w_{fm}}{1 - w_{fm}} \quad \text{Eq. (7)}$$

2.3.2. Viscoelasticity vs. poroelasticity of the hydrogels

To investigate whether the different hydrogels are of viscoelastic or poroelastic nature, the hydrogels were indented by two spherical probes of different diameters (1 mm and 2 mm). The premise is that the measured mechanical properties of the hydrogel is independent of the indenter size if the applied strain field and strain rate remain constant (Fung et al., 2017). The strain field resulting from the spherical indenters of different sizes can be made equivalent by keeping the ratio of

indentation depth to indenter radius constant (Wahlquist et al., 2017). The strain rate was controlled to match the underlying mechanisms of viscoelasticity and poroelasticity. For a viscoelastic material, the loading rate depends on the loading rise time (t_{rise}); whereas for a poroelastic material, the loading rate depends on the probe size, and is defined as $\dot{\delta}r$. In the current study, the loading rates for 1 mm- and 2 mm-diameter indenters were matched for either the viscoelastic rate ($\frac{1}{t_{rise}}$) or the poroelastic rate ($\dot{\delta}r$). The ratio of the effective contact modulus measured by the two indenters were evaluated. If a material is viscoelastic (poroelastic), the effective contact modulus ratio is equal to 1.0 when the matched viscoelastic (poroelastic) rate is used. A table detailing the indentation depths and rates for different indenter sizes is included in the Supplementary Materials S1.

2.3.3. FE model-driven numerical optimisation for material parameters using unconfined compression data

The hydrogel was modelled as a fibre-reinforced poroelastic biphasic material consisting of a porous solid saturated with fluid and reinforced by fibres with continuous random (i.e., spherical) distribution (Meloni et al., 2017; Moo et al., 2022). The fibre bundle can only resist tension. The strain potential function of the fibre bundle is described by a power law with a fibre modulus, ξ, and an exponent set at 2 (Eq. (S6)). The ground matrix was modelled as a compressible neo-Hookean solid, which was characterised by the Young's modulus, E, and Poisson's ratio, ν (Eqs. (S3) – (S5)). The solid fraction, φ_s followed the w/v composition of the hydrogels (0.04 for alginate and agarose; 0.15 for GelMA). The fluid flow in the solid obeys the Darcy's law, with the hydraulic permeability assumed to be isotropic and deformation-dependent and defined by k_0 and M, respectively (Eq. (S12)). The constitutive equations used for the solid and fluid phases are included in the Supplementary Materials S8.

An open source FE software FEBio (v.3.7.0) was used to perform the FE simulation and numerical optimisation. A quarter of a cylindrical-shaped FE model was constructed based on the hydrogel geometry, and discretized into pentahedral and hexahedral elements. A mesh of 300 elements was created, with the mesh biased towards smaller size from the centre to the lateral surface along the radial direction. The final mesh size was determined by a mesh convergence analysis (see Supplementary Materials S6). Unconfined compression of 10% nominal strain at a loading rate of 2 μm/s and stress relaxation at the target strain for 30 min was simulated. Frictionless biphasic contact was assumed for the top surface. The bottom surface was restricted only along the vertical direction. The lateral surface was assumed to be free-draining with fluid pressure set at zero. The xz- and yz-symmetric planes were restricted against displacement along y- and x-directions, respectively (see Supplementary S7 for further details).

A set of five material parameters (E, ν, ξ, k_0 and M) were obtained by curve-fitting the simulated force-time curve to that collected from unconfined compression of hydrogels. The numerical optimisation of material parameters was performed using FEBio's built-in least-square parameter optimisation routine, based on the Levenberg-Marquardt algorithm (Maas et al., 2012). An educated initial guess of the material properties was provided. The convergence tolerance for objective function was set to 10^{-5}. The coefficient of determination, r^2, was determined for every converged solution, and only those with $r^2 \geq 0.80$ were accepted as solutions.

Following the numerical optimisation procedure, the unconfined compression was simulated using the optimised material parameters to determine the average fluid load fraction, w_f, at the instant of peak load. The w_f obtained from FE simulation is defined as the ratio of fluid pressure to contact pressure averaged over the top hydrogel surface. The compressive modulus was determined from the slope of the stress-strain curve at a nominal strain of 8%. In addition, a separate hydrogel model with the same geometry but a denser mesh was constructed, characterised by the optimised material parameters, and used for an in-silico tensile test to determine the tensile modulus of the hydrogels at the nominal strain of 8% (see Supplementary Materials S7 for more details). The tension-compression modulus ratio, ζ_E, was determined by dividing the tensile modulus by the compressive modulus.

In order to evaluate the consistency of the numerical optimisation procedure in identifying the optimised material properties, the same optimisation procedure was run for ten times by using ten different initial guesses of the material parameter set (E, ν, ξ, k_0 and M). Each of the five material parameters was randomly selected from a reasonable parameter-specific range for the initial guess. The coefficient of variation (CV) was determined for every material parameter as the standard deviation divided by the mean calculated from the results of the ten runs. A material parameter with a low CV is more consistently determined by the numerical optimisation procedure than the one with a high CV. The CVs of the w_f and ζ_E that corresponded to the optimised parameter sets were also determined.

For every set of optimised material parameters, a deviation-from-mean score, χ, was calculated:

$$\chi_i = (1 - r^2)\left(\left|\frac{E_i - E_m}{E_m}\right| + \left|\frac{\nu_i - \nu_m}{\nu_m}\right| + \left|\frac{\xi_i - \xi_m}{\xi_m}\right| + \left|\frac{k_{0i} - k_{0m}}{k_{0m}}\right| + \left|\frac{M_i - M_m}{M_m}\right|\right) \quad \text{Eq. [8]}$$

where the subscript i indicates the current set of material parameters, and

the subscript m is the mean value of a specific parameter determined from the ten runs.

The sets of optimised material parameters with the lowest χ score, together with their corresponding w_f and ζ_E, were reported.

2.4. Statistical analysis

The material parameters derived by curve-fitting to the indentation data (E_c, E_{c0}, E_{cp}, w_{fm}, k_0) and to the unconfined compression data (E, ν, ξ, k_0, M) were included as long as the $r^2 \geq 0.80$. The material properties that were subsequently derived from the curve-fitted parameters were w_f, ζ_E for indentation and unconfined compression. All data were presented as estimated marginal mean (EMM) ± 95% confidence interval (CI). A commercial statistical software SPSS (v27, IBM Corp, Armonk, NY) was used for the statistical analyses. A generalised estimating equation (GEE, under Genlin procedures in SPSS) was used to compare the material parameters of different hydrogel systems (i.e., GelMA, agarose, and alginate) with and without reinforcement by the MEW fibrous meshes (i.e., fr and nonfr) to account for the unequal number of sample size between groups as some of them failed the inclusion criterion of $r^2 \geq 0.80$. Likewise, the effective contact modulus ratio at matched viscoelastic and poroelastic strain rates obtained for different hydrogels were also assessed for difference from one by Genlin procedures. In addition, Genlin Mixed procedures were used to analyse for the effects of hydrogel type and indentation location (i.e., no-fibre, unifibre, and cross-fibre regions) for the fr hydrogels. Multiple comparisons underwent LSD adjustment. All statistical tests were two-sided with the type I error set at 0.05.

3. Results

The 4% agarose and alginate hydrogels were mechanically superior to the 15% GelMA (Fig. 2). The agarose and alginate have higher E_{c0} (by 39% and 90%), E_{cp} (by 219% and 256%), w_f (by 242% and 205%), w_{fm} (by 85% and 90%), and ζ_E (by 355% and 394%) than the GelMA. Inclusion of MEW meshes increased the near equilibrium and peak contact moduli of all hydrogels, but by a magnitude that was hydrogel-dependent. The E_{c0} and E_{cp} of the fr-GelMA was 312% and 494% higher than the nonfr-GelMA; whereas agarose and alginate samples showed 70–156% increase for the E_{c0}, but only a slight increase (30–34%) for the E_{cp} after being reinforced by MEW meshes (Fig. 2A–B).

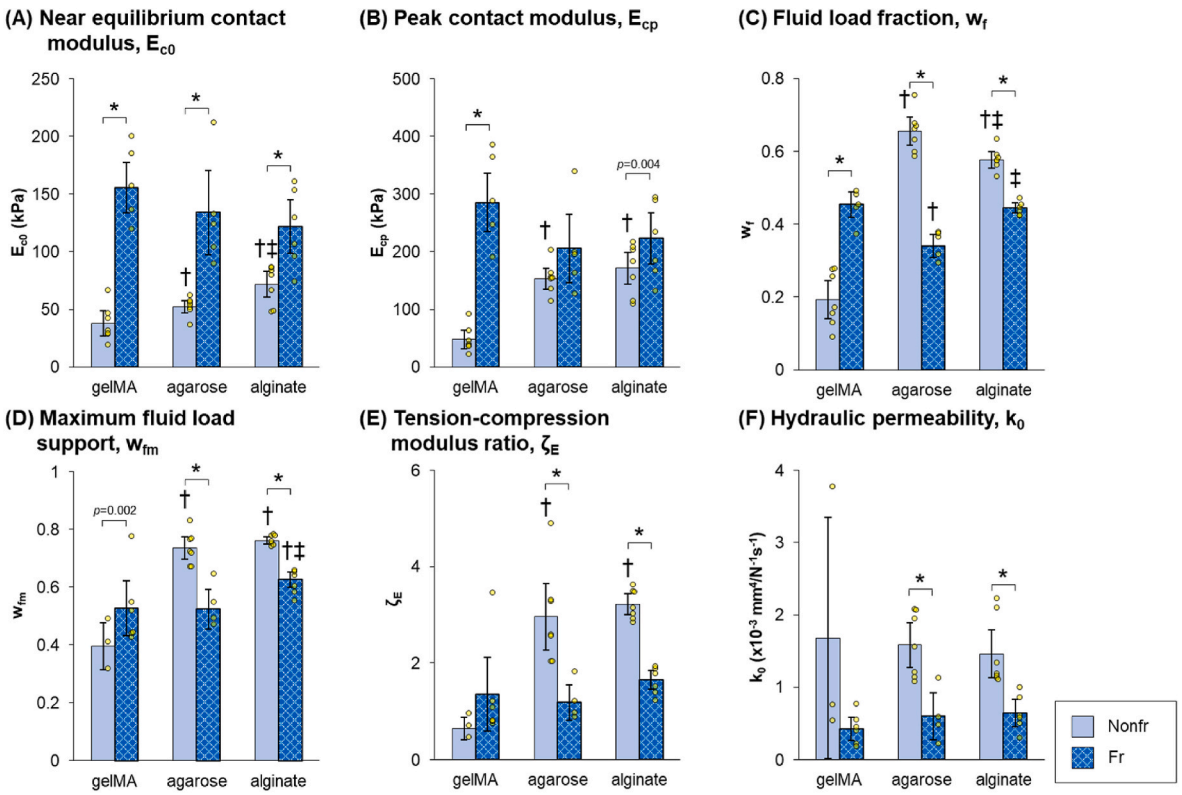

Fig. 2. Reinforcing effects of MEW fibrous meshes on the material properties of three hydrogel systems (GelMA, agarose and alginate). The material parameters were derived by curve-fitting the indentation data to a biphasic Hertzian model for nonfr- and fr-hydrolges. The fr-hydrogels were indented over the no-fibre region (see Fig. 1A). (A) Near equilibrium contact modulus, E_{c0}, (B) peak contact modulus, E_{cp}, (C) fluid load fraction, w_f, (D) maximum fluid load fraction, w_{fm}, (E) tension-compression modulus ratio, ζ_E and (F) hydraulic permeability, k_0. * indicates significant difference between the fr and nonfr conditions for a specific hydrogel ($p < 0.001$). † and ‡ denote significant difference with GelMA and agarose, respectively, for the corresponding fibre reinforcement condition (nonfr and fr, $p < 0.05$).

The disproportionate increase in E_{c0} and E_{cp} led to different changes to the w_f, w_{fm}, and ζ_E. For GelMA, the MEW reinforcement increased the fluid load fraction by 135% (Fig. 2C). The w_{fm} and ζ_E of the fr-GelMA were also similarly improved by 33%, and by 109%, respectively (Fig. 2D–E). In contrast, the w_f degraded from 0.65 to 0.34 for agarose, and from 0.58 to 0.45 for alginate after the inclusion of MEW meshes. Correspondingly, the w_{fm} and ζ_E of fr-agarose and fr-alginate became significantly lower than their nonfr counterparts. The hydraulic permeability of fr-agarose and fr-alginate were 62% and 56% lower than the nonfr-agarose and nonfr-alginate, respectively (Fig. 2F). Overall, the contact modulus (E_{c0}, E_{cp}), and tension-compression modulus ratio were comparable across all fr-hydrogels.

The local reinforcing effects of MEW meshes were measured by indenting the fr-hydrogels over the no-fibre, uni-fibre and cross-fibre regions. For the fr-GelMA, there were no significant differences in material properties found between different regions (Fig. 3). For the fr-agarose, the maximum fluid load support at the cross-fibre region was 26% higher than at the no-fibre region (Fig. 3C). Correspondingly, the ζ_E measured at the cross-fibre region was 93% higher than at the no-fibre region (Fig. 3D). The fluid load fraction of fr-agarose at $\delta = 100$ μm was 0.35–0.37 in all tested regions, which were 29–36% lower than the corresponding regions in fr-GelMA and fr-alginate (Fig. 3B). For the cross-fibre region of the fr-alginate, the effective contact modulus was 37–52% higher (Fig. 3A), but the hydraulic permeability was 64% lower (Fig. 3E), when compared with the no-fibre and the uni-fibre regions. The w_f at the no-fibre region of fr-alginate was approximately 39% higher than at the uni-fibre and cross-fibre regions.

DEPTH trials showed an exponential decrease of E_c with increasing indentation depth (Figs. S1 and S2). When the indentation order was reversed for depths of 150 μm and 200 μm, the E_c measured at 150 μm was lower than that at 200 μm for most indented regions (except for the nonfr-GelMA and nonfr-alginate), which contradicted the exponential dependence of E_c on indentation depth (Figs. S1-S2) and was likely caused by the reversed indentation order. Therefore, the E_c at 150 μm was corrected by fitting the E_c-δ data (excluding the data of E_c at 150 μm) to an exponential function $E_c = ae^{-b\delta} + c$, where a, b, c were the fitting constants. It was determined that the E_c at 150 μm was decreased by approximately 21% due to the reversed indentation order (Fig. S3 and Table S2). The fluid load fraction was also found to depend on the indentation depths. The w_f generally decreased with increasing indentation depth. We note that the w_f determined by the peak and near-equilibrium contact moduli through Eq. (5b) generally reflected the w_f measured at the greatest indentation depth of 250 μm (Figs. S4 and S5).

The hydrogels were indented by two indenter sizes at matched strain fields and rates to investigate the origin of the time-dependent mechanical properties. For the nonfr-hydrogels, GelMA and alginate were found to be viscoelastic by a small margin; whereas agarose were neither viscoelastic nor poroelastic (Fig. 4A, see Methods for more details). For the fr-hydrogels, visco- and poro-elasticity both contributed to the time-dependent mechanics without clear dominance of either mechanism. The only exceptions were fr-alginate indented over the uni-fibre region (Fig. 4C), and fr-GelMA indented over the cross-fibre region in which they were found to be mainly viscoelastic (Fig. 4D).

The macroscale material properties were successfully determined from the unconfined compression data by a FE model-driven optimisation procedure (Fig. 5). For the non-fr hydrogels, the Young's modulus of agarose was highest at 34 kPa, compared to 14 kPa of GelMA and 9 kPa of alginate (Fig. 5A). The fibre modulus of agarose was also highest at 3.8 kPa, in comparison with the negligible 0.1 kPa found in GelMA, and the 1.1 kPa in alginate (Fig. 5C). Correspondingly, the tension-

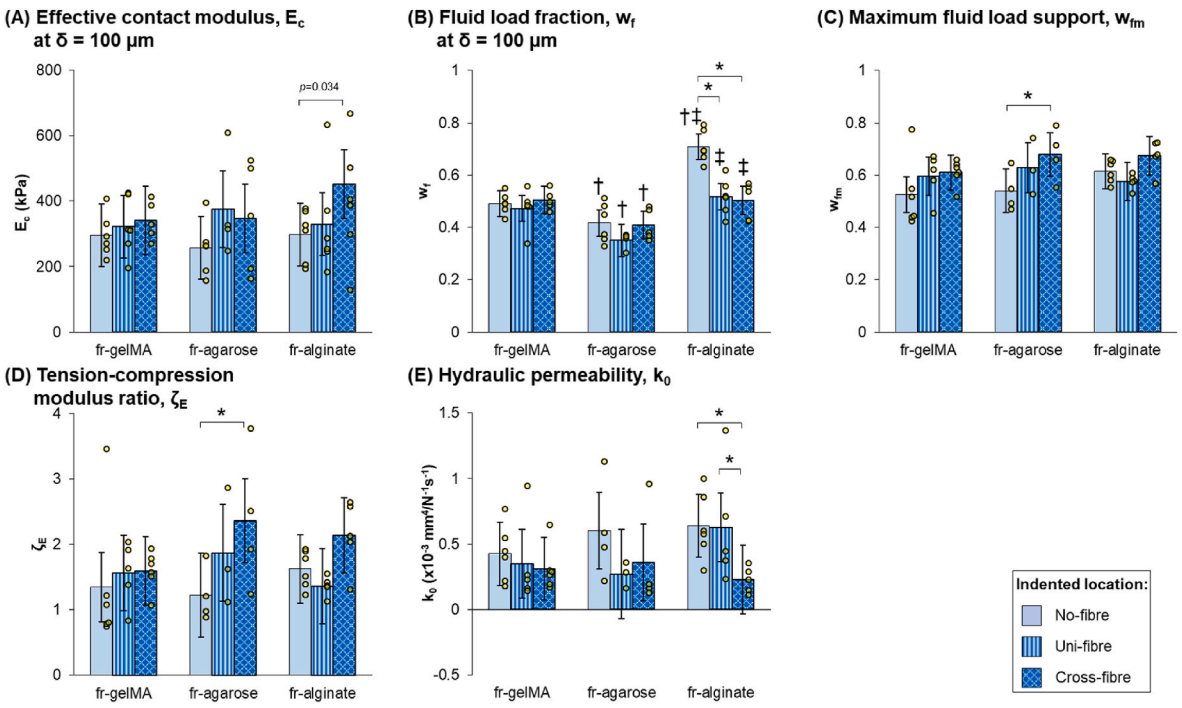

Fig. 3. Mechanical properties of fr-hydrogels measured over no-fibre, uni-fibre and cross-fibre regions to investigate the local reinforcing effects of MEW meshes with 600 μm fibre spacing. (A) The effective contact modulus, E_c and (B) the fluid load fractions, w_f, were measured from the indentation of hydrogels to a depth of 100 μm at a loading rate of 8 μm/s (DEPTH trials, see Fig. 1A). (C) The maximum fluid load support, w_{fm}, (D) tension-compression modulus ratio, ζ_E and (E) hydraulic permeability, k_0, were measured by indenting the hydrogels to a depth of 125 μm at increasing loading rates that ranged from 0.5 to 20 μm/s (RATE trials, see Fig. 1A). * indicates significant difference between the no-fibre, uni-fibre and cross-fibre regions for a specific hydrogel ($p < 0.05$). † and ‡ denote significant difference with GelMA and agarose, respectively, for the corresponding indented regions ($p < 0.05$).

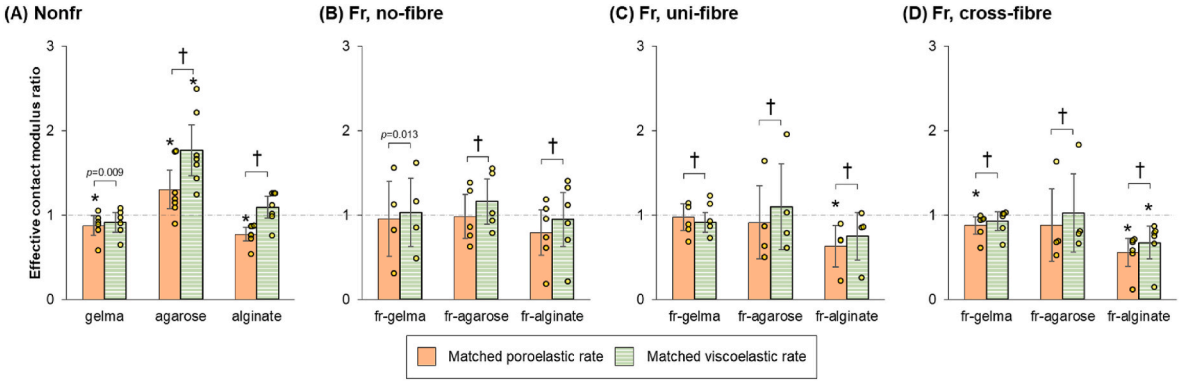

Fig. 4. The ratio of effective contact modulus measured by an indenter of 2 mm diameter to that by a 1 mm-diameter indenter at matched strain field, and matched viscoelastic or poroelastic rate. The ratios were measured for (A) nonfr hydrogel, (B) fr-hydrogel at no-fibre region, (C) fr-hydrogel at uni-fibre region, and (D) fr-hydrogel at cross-fibre region. A hydrogel is viscoelastic (or poroelastic) if the effective contact modulus ratios were not different from 1.0 when measured at matched viscoelastic (or poroelastic) rate (see Section 2.3.2 for more details). Note that as the E_c measured by 1 mm-diameter probe at indentation depth of 150 μm was generally reduced by the indentation order effect, the measured E_c at 150 μm depth was corrected by an exponential fitting to E_c-δ data (see Results and Supplementary Materials S2 – S3 for more details). * indicates significant difference from 1.0 ($p < 0.05$), and † denotes significant difference between the compared groups ($p < 0.001$).

compression modulus ratio and fluid load fraction were higher for agarose (ζ_E: 1.6, w_f: 0.49) and alginate (ζ_E: 1.8, w_f: 0.56) than for GelMA (ζ_E: 1.3, w_f: 0.34) (Fig. 5F–G). There were no significant differences in Poisson's ratio and hydraulic permeability between non-fr hydrogels, with values ranging from 0.16 to 0.19 for ν (Fig. 5B) and from 0.15 to 0.40 $mm^4N^{-1}s^{-1}$ for k_0 (Fig. 5D), respectively. Agarose had higher M factor of 25 than GelMA (4.3) and alginate (9.9) (Fig. 5E). Following the reinforcement by the MEW meshes, the Young's modulus was improved for all hydrogel systems, with 213%, 92%, and 219% increase for GelMA, agarose and alginate, respectively. Interestingly, only the fibre modulus of fr-GelMA was enhanced from 0.1 kPa to 4.1 kPa. The fibre modulus of fr-alginate did not change; whereas the fibre modulus of fr-agarose was 64% lower at 1.4 kPa than its nonfr counterparts. The tension-compression modulus ratio of fr-agarose was 31% lower than nonfr-agarose, and was lowest at 1.1 among fr-GelMA (1.5) and fr-alginate (1.5). The fluid load fraction also degraded from 0.49 to 0.28 for agarose and from 0.56 to 0.39 for alginate following the inclusion of MEW meshes. For GelMA, MEW reinforcement improved the fluid load fraction by 82%, from 0.34 in nonfr-to 0.62 in fr-GelMA (Fig. 5G). The hydraulic permeability showed trend of lower values in all hydrogels

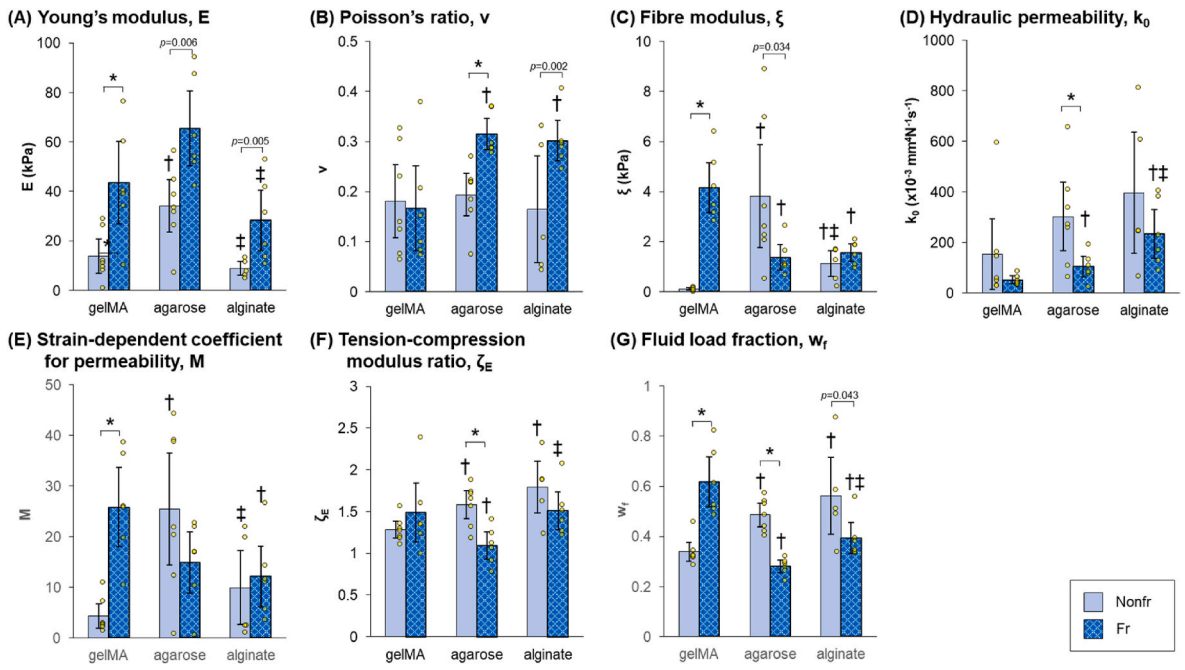

Fig. 5. Material parameters obtained by FE model-driven numerical optimisation procedure using data collected from the unconfined compression of three hydrogel types with and without MEW fibrous reinforcement. The material parameter set containing (A) Young's modulus, E, (B) Poisson's ratio, ν, (C) fibre modulus, ξ, (D) hydraulic permeability, k_0, and (E) strain-dependent coefficient for permeability, M, was determined by the optimisation procedure, and with lowest deviation-from-mean χ score (see Eq. (8)); whereas (F) tension-compression modulus ratio, ζ_E and (G) fluid load fraction, w_f, represent the corresponding mechanical behaviour of the optimised hydrogel models. * indicates significant difference between the fr and nonfr conditions for a specific hydrogel ($p < 0.001$). † and ‡ denote significant difference with GelMA and agarose, respectively, for the corresponding fibre reinforcement condition (nonfr and fr, $p < 0.05$).

reinforced by MEW meshes, but only fr-agarose showed statistically significant decrease. The M factor of fr-agarose and fr-alginate were not different from their nonfr counterparts. However, the M factor of the fr-GelMA (26) was higher than that of the nonfr-GelMA (4.3). The Poisson's ratio of fr-agarose and fr-alginate was higher than their nonfr counterparts by 68–88%, whereas reinforcement of GelMA by MEW meshes did not change the Poisson's ratio.

Of the five parameters fitted by FE-driven optimisation, only Young's modulus of narrow range was consistently predicted, with CV ranging from 4.4 to 31% for all hydrogels (Fig. 6A). There were large variations for the optimised ν, ξ, k_0, with CV of 34–98, 26–72 and 31–84%, respectively, across all hydrogels (Fig. 6B–D). The CV of M factor was the highest at 51–123% for all hydrogels (Fig. 6E). Nevertheless, the mechanical behaviour of the optimised material models (*i.e.*, ζ_E and w_f)

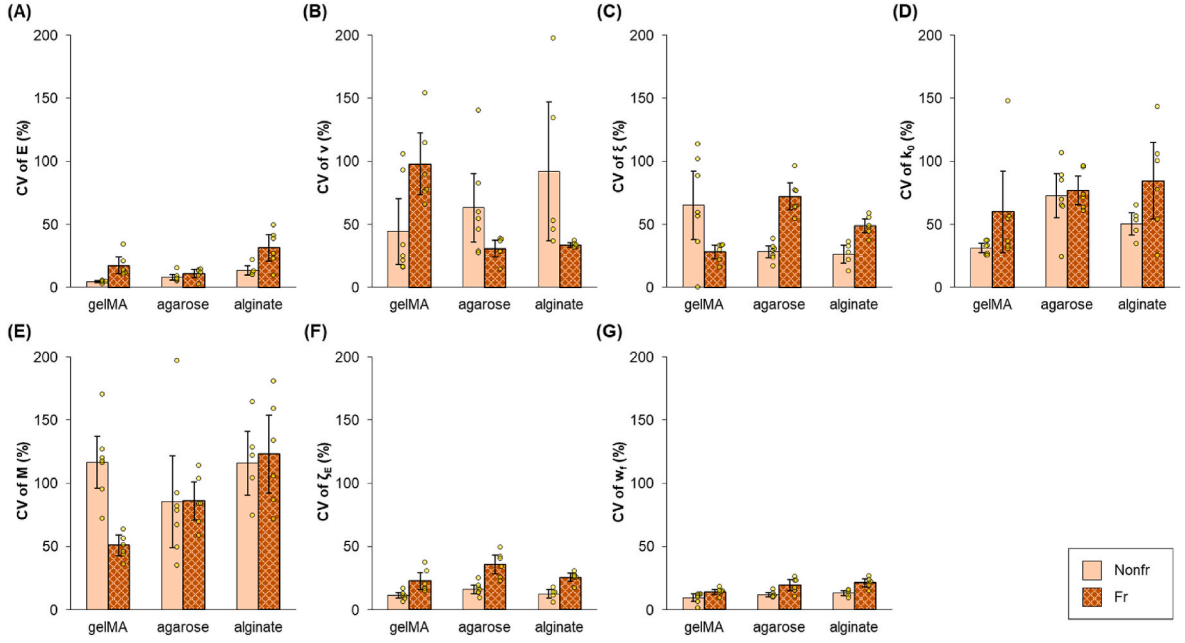

Fig. 6. Consistency of the FE model-driven optimisation procedure in predicting the material parameters using the unconfined compression data, measured in terms of coefficient of variation (CV). The CV of (A) E, (B) ν, (C) ξ, (D) k_0, (E) M, (F) ζ_E and (G) w_f were presented. The parameters with a low CV have high consistency. Note that statistical comparisons between groups were not marked as they offer no additional value for data interpretation.

showed relatively high consistency. The CV of ζ_E was 11–36% (Fig. 6F), while the CV of w_f was 9–21% (Fig. 6G) across all hydrogels.

4. Discussion

This study examined the effect of MEW meshes on reinforcing three hydrogel systems with different compositions and structures. Compositionally, GelMA hydrogels are protein-based and contain integrin-binding motif Arg-Gly-Asp (RGD), which promotes cell adhesion (Yue et al., 2015). Alginate and agarose hydrogels are carbohydrate-based (Lee and Mooney, 2012; Roach et al., 2016). The anionic nature of alginate hydrogels mimics the fixed charge density present in the extracellular matrix of various connective tissues. Agarose, however, is uncharged and intrinsically inert. Structurally, these porous hydrogels have an average pore size that is estimated to differ by four orders of magnitude based on the hydrogel concentration used in the current study, ranging from 24 μm for GelMA (Chen et al., 2012), to 0.2 μm for agarose (Pernodet et al., 1997), and to 0.005 μm for alginate (Boontheekul et al., 2005). We found that the time-dependent mechanical behaviour of the tested hydrogel systems were contributed by both visco- and poro-elastic mechanisms, whose dominance cannot be clearly distinguished by our testing method (Fig. 4). As poro-elasticity constitutes the basis of the mechanics for the tested hydrogels, fluid pressure likely developed in these hydrogels when they are mechanically loaded. In view of that, we used the biphasic material model, which is based on the theory of poroelasticity and considers hydrogels as materials composed of solid and fluid phases, for the extraction of material properties of the hydrogels by micro-indentation and unconfined compression. Following the data analysis, we discovered that (i) load-induced fluid pressurisation following the incorporation of MEW meshes increased only for GelMA hydrogel, but decreased for agarose and alginate hydrogels, (ii) Incorporation of MEW meshes into the hydrogels did not lead to mechanical heterogeneity for length scale ranging from 50 to 250 μm, (iii) material properties derived by micro-indentation and unconfined compression agree with each other despite the fact that they used different boundary conditions and derived based on different theoretical models (*i.e.*, biphasic Hertz vs. biphasic mixture), (iv) except for the Young's modulus, most material parameters determined for the hydrogels with and without MEW meshes showed great variation over repeated runs. Nevertheless, the overall mechanical behaviours of the optimised material model, as measured in terms of fluid load fraction and tension-compression modulus ratio, were predicted with relatively low variability.

Load-induced fluid pressurisation plays an important role in enhancing the transient mechanical stiffness of a fluid-saturated porous material. In connective tissue such as articular cartilage, interstitial fluid takes up > 90% of the applied load during the transient phase, which not only enhances the mechanical stiffness, but also protects the solid phase from overloading and enhances the lubrication of the cartilage (Ateshian, 2009; Bonnevie et al., 2012; Moo et al., 2021). In addition to mechanical benefits, effective fluid pressurisation during mechanical loading also generates microenvironment of high hydrostatic pressure that acts as a mechanical stimulus for the regulation of metabolism of the embedded cells. Hydrostatic pressure at a magnitude of 40–100 kPa has been shown to up-regulate protein production of cells (Gavénis et al., 2007; Luo and Seedhom, 2007; Miyanishi et al., 2006) in a dose-dependent manner (Elder and Athanasiou, 2009; Gavénis et al., 2007). Using the measured contact pressure and fluid load fraction, we estimated that agarose and alginate generated high fluid pressure ranging from 22 to 46 kPa for nominal strains of 2.5–12.5%, compared to the negligible 4–5 kPa in GelMA for the same magnitudes of indentation (Table 1, Supplementary Material S9). When the MEW meshes were incorporated, the load-induced fluid pressurisation was significantly enhanced for GelMA (by 5–11 times), slightly improved for alginate (−3 – 19%), but decreased for agarose (by −8 to −33%,

Table 1
Fluid pressure at different indentation depth. For the fr-hydrogels, the fluid pressure at the no-fibre region was reported (see Supplementary Materials S9 for more details).

	Fluid pressure at different indentation depth (kPa)				
	50 μm	100 μm	150 μm	200 μm	250 μm
Nonfr-GelMA	4.1	5.3	4.0	5.1	5.3
Nonfr-agarose	21.7	31.3	35.4	44.0	45.6
Nonfr-alginate	26.8	41.6	40.5	40.5	45.8
Fr-GelMA	28.7	39.9	43.7	48.4	63.8
Fr-agarose	20.0	24.4	23.8	33.0	33.3
Fr-alginate	31.8	45.0	39.2	44.8	47.5

Table 1). Hydraulic permeability and tension-compression non-linearity of the hydrogels are the two primary factors governing the load-induced fluid pressurisation (Bonnevie et al., 2012; Moore et al., 2015). Specifically, hydrogels with low hydraulic permeability and high tension-to-compression modulus ratio develop high transient fluid pressure when compressed. Our results showed that the MEW meshes had consistent effect on the average permeabilities over all hydrogels (*i.e.,* reduction by 56–75%), but affected the tension-to-compression modulus ratio in a hydrogel-dependent manner. Indeed, the tension-to-compression modulus ratio was increased only for GelMA, but decreased for agarose and alginate following the incorporation of MEW meshes (Fig. 2F). Therefore, the key to improving the load-induced fluid pressurisation depends on the effectiveness of the MEW meshes in enhancing the tension-compression modulus ratio of the hydrogel system.

Tension-compression nonlinearity is a distinct mechanical feature of various fibre-reinforced connective tissues, such as articular cartilages, menisci, and intervertebral discs (Moo et al., 2021; Ateshian et al., 2009; Chahine et al., 2004), which describes the disproportionately high tensile stiffness of the material relative to the corresponding compressive stiffness. In articular cartilage, for example, the tensile-to-compression modulus ratio can be as large as 9 (Bonnevie et al., 2012). Polysaccharide-based hydrogels, such as agarose, form semi-flexible fibrillar network following cross-linking (Ed-Daoui and Snabre, 2021; Bertula et al., 2019). Previous studies have shown that agarose hydrogels have tensile stiffness that is approximately three times higher than the compressive stiffness (Kelly et al., 2013). Consistent with previous findings, we found tension-compression modulus ratio of approximately 3 for agarose (2.96) and alginate (3.21) hydrogels. GelMA hydrogel, however, is stiffer in compression than in tension with ζ_E of 0.65 (Fig. 2). The incorporation of MEW meshes reversed this behaviour for GelMA and gave fr-GelMA a tension-compression modulus ratio of 1.35, thus suggesting a greater enhancement of tensile stiffness than the compressive stiffness by MEW meshes (Fig. 2). To our surprise and contrary to our hypothesis, we found that the MEW meshes did not reinforce agarose and alginate by the same mechanism observed for GelMA, as the ζ_E degraded from approximately 3 to 1.65 for alginate and to 1.18 for agarose, respectively. We speculate that the different cross-linking mechanisms used by these hydrogels could explain the varying reinforcement of the embedded MEW meshes. GelMA hydrogels are cross-linked by strong covalent bonds, which are not easily broken (Yue et al., 2015; Bartnikowski et al., 2015) and therefore more likely to mechanically tense the embedded MEW meshes during compressive loading. Alginate and agarose hydrogels used in the current study are ionically and physically crosslinked, respectively. The ionic and physical bonds are weaker bonds than covalent bonds and are prone to breakage under deformation. Although the agarose and alginate hydrogels prevented the buckling of the MEW meshes, as evidenced by the increase of near-equilibrium modulus and Young's modulus, these hydrogels were not able to effectively tense the embedded MEW meshes during mechanical loading, which ultimately led to disproportionate changes to their tensile and compressive stiffnesses by the MEW mesh.

Furthermore, the embedded MEW meshes may interfere with the formation of tertiary structures within the polysaccharide-based hydrogels and affect the overall mechanical properties of the fr-hydrogels (Rees and Welsh, 1977). The reinforcing mechanism of MEW meshes in terms of load-induced fluid pressurisation warrants further investigations by using hydrogel system that can be ionically and covalently cross-linked, such as the alginate hydrogel (Lee and Mooney, 2012).

The localised mechanical properties were investigated by indenting the hydrogels to different depths at different loading rates. Consistent with previous findings (Roach et al., 2016; Ed-Daoui and Snabre, 2021; Bertula et al., 2019), we found a compressive strain-softening behaviour in all hydrogels with and without the embedment of MEW meshes, with their effective contact moduli showing exponential decrease with increasing strains. Interestingly, the fluid load fraction in these hydrogels also exhibited the similar decrease with increasing compressive strains. We note that the hydrogels could also show strain-stiffening behaviour, but this behaviour was limited to hydrogels that were cross-linked *in situ* at the rheometer and underwent shear loading (Bertula et al., 2019; Hashemnejad and Kundu, 2016). For the tested length scale of 50–250 μm, we found that the MEW meshes did not introduce measurable mechanical heterogeneity. However, mechanical heterogeneity may be present for length scales smaller than those studied here, and should be investigated further through nano- or micro-scale mechanical testing systems with high sensitivity, such as atomic force microscopy (Markert et al., 2013).

The indentation tests were conducted on an order of increasing depth for depths ranging from 50 to 250 μm. By reversing the indentation order for the depths of 150 μm and 200 μm, we found a considerable reduction of effective contact modulus for agarose and all fr-hydrogels at the depth of 150 μm that cannot be attributed to the strain-softening behaviour described above (see Supplementary Materials S2 – S3). Furthermore, the loading path of the subsequent indentation to 250 μm depth followed that of the softened 150 μm indentation, rather than that of the 200 μm indentation (Figs. S6 and S7). This stress-softening behaviour is indicative of the Mullins effect (Mullins, 1947; Ogden and Roxburgh, 1999) and suggests an inelastic deformation of the MEW-mesh-reinforced hydrogels and agarose hydrogels. For the agarose hydrogels, it is likely that the physical cross-links within the hydrogel were broken during deformation and reformed at the newly deformed state. Likewise, there may be breakages and re-formations of linkage between the embedded MEW mesh and the hydrogels for the fr-hydrogels following indentation to a specific depth. It should be noted that despite showing Mullins effect, the following indentation of the hydrogels is elastic so long as no additional magnitude of indentation is applied (Mullins, 1947; Ogden and Roxburgh, 1999). Importantly, we emphasize that the measured fluid load fractions of all hydrogels with and without the reinforcement by MEW meshes (Figs. S4 and S5), and thus the load-induced fluid pressurisation (Table 1), were not affected by the indentation order.

Although using different boundary conditions, the relative changes of material properties due to fibre reinforcement obtained through indentation generally agreed with those obtained by unconfined compression. Specifically, we found that the incorporation of MEW meshes led to an increased equilibrium modulus and a decreased hydraulic permeability for all hydrogels, independent of the mechanical test methods used (Figs. 2 and 5). Agreement in material properties derived through indentation and unconfined compression was also found in previous studies (Meloni et al., 2017). Importantly, we arrived at the same conclusion regarding the changes to the load-induced fluid pressurisation and the tension-compression modulus ratio brought upon by the incorporation of MEW meshes into GelMA, agarose and alginate hydrogels despite using different mechanical testing methods (indentation vs. unconfined compression) that were coupled to different theoretical models (biphasic Hertz analytical vs. biphasic fibre-reinforced FE models). The material parameters derived in the current study are also consistent with those reported in the literature. For example, the measured Young's modulus of ~34 kPa for 4% agarose (Fig. 5A) was comparable to those reported by Meloni et al. [their Fig. 8A]. Interestingly, we found that the hydraulic permeability obtained by indentation and unconfined compression differed by approximately two orders of magnitude (10^{-3} vs 10^{-1} $mm^4N^{-1}s^{-1}$, Fig. 2F vs. Fig. 5D). This is likely due to the different assumptions employed by the different theoretical models used for curve-fitting. The biphasic Hertzian model assumes constant permeability whereas the biphasic fibre-reinforced mixture model assumes deformation-dependent permeability. Therefore, it is crucial to consider the model assumptions and boundary conditions used when making direct data comparison. For example, the hydraulic permeability of 15% GelMA measured by indentation, as reported by Miri et al. [their Fig. 3B], was comparable to the permeability values derived by indentation in this study (Fig. 2F). Likewise, the hydraulic permeability of 4% agarose hydrogels obtained by unconfined compression in our study are also consistent with those measured by direct permeation experiment on 2% agarose (Soltz et al., 1999) after accounting for a reduction of permeability by approximately one order of magnitude when the agarose concentration was increased from 2% to 4% w/v [Gu et al., 2003, their Fig. 2]. Finally, we note that Meloni et al. (2017) reported hydraulic compression of agarose hydrogels that was one order of magnitude greater than the value reported in our study (200 vs 20 $mm^4N^{-1}s^{-1}$) despite using the same test set-up of unconfined compression. This difference was likely caused by the assumption of constant permeability in the Meloni et al. study, as opposed to the deformation-dependent permeability used in the current study.

For the FE model-driven numerical optimisation procedure, we found that except for Young's modulus, the optimised solutions for the other four material parameters (*i.e.*, ν, ξ, k_0, M) showed great variation, with CV ranging from 28 to 123% (Fig. 6). This suggests that the optimised solutions for four out of the five fitted parameters were not unique, and that there are multiple local minima in our non-convex optimisation problem that did not necessarily represent the global minimum (Townsend et al., 2016). Nevertheless, the resulting mechanical behaviour of the optimised model (*i.e.*, w_f and ζ_E), from which the conclusion of the current study is drawn, showed reasonable consistency over the ten runs with CV of 9–36% (Fig. 6).

There are limitations in our study that should be considered. First, we only tested a specific concentration for each hydrogel system. These hydrogel concentrations were chosen to ensure reliable force measurements with our material testing system. The extent of load-induced fluid pressurisation may vary for hydrogels of different concentrations and will form the subject of our future studies. Second, the theoretical models used for the fitting of material parameters did not take into account the Mullins effect. Phenomenological model accounting for the Mullins effect (Ogden and Roxburgh, 1999) may be considered in future studies to improve the accuracy of the material parameter fitting procedure. Finally, it should be pointed out that the good agreement of the results obtained from indentation and unconfined compression suggests that the tested hydrogels exhibited homogeneous material properties independent of the MEW mesh incorporation. The same agreement likely does not apply to specimens with known material inhomogeneity, such as cartilages and menisci, or growing TE construct showing inhomogeneous protein deposition.

5. Conclusion

We conclude that MEW meshes reinforce the GelMA hydrogels by increasing their equilibrium compressive stiffness, and load-induced fluid pressurisation. The improvement in fluid load support may be due to the ability of the GelMA hydrogel, which is covalently cross-linked, in tensing the embedded MEW meshes during mechanical compression. This is supported by a concomitant increase of the tension-to-compression modulus ratio from 0.6 to 1.3 following the

incorporation of MEW meshes into GelMA hydrogel. Covalent cross-linking in the hydrogels may be crucial for the mechanical reinforcement by MEW meshes, as significant reduction of tension-to-compression modulus ratio and load-induced fluid pressurisation were observed for non-covalently cross-linked hydrogels, such as agarose and alginate following the incorporation of MEW meshes. The fluid pressure induced in fr-GelMA (30–60 kPa) by physiologically relevant strain (12.5%) could serve as a potent mechanical stimulus for the embedded cells, and together with the compressive and/or shear mechanical stimuli, could accelerate the process of cell growth. The potential of tuning the load-induced pressurisation in hydrogels by MEW meshes of different designs should be explored further. Micro-indentation and unconfined compression produced biphasic material properties that are consistent with each other, and therefore represent two useful approach for the mechanical characterisation of hydrogels. The methods developed in this study are able to tease out the contribution of solid and fluid constituents of the hydrogels to the overall mechanical properties of the constructs, and thus serve as useful tools for the design of MEW meshes for tuning the load-induced pressurisation in the cell-embedding hydrogels.

Funding resources

We would like to acknowledge the financial supports from the Marie Skłodowska-Curie Actions postdoctoral fellowship (project number: 890936), Academy of Finland (grant 324529), the Dutch Arthritis Society (LLP-12 and LLP-22), the Gravitation Program “Materials Driven Regeneration”, funded by the Netherlands Organization for Scientific Research (024.003.013), the Reprint project (OCENW.XS5.161) funded by the Netherlands Organization for Scientific Research, and the Carleton University internal research start-up fund (186725).

CRediT authorship contribution statement

Eng Kuan Moo: Writing – review & editing, Writing – original draft, Visualization, Validation, Software, Project administration, Methodology, Investigation, Funding acquisition, Formal analysis, Data curation, Conceptualization. **Mohammadhossein Ebrahimi:** Writing – review & editing, Methodology, Investigation, Data curation. **Andrei Hrynevich:** Writing – review & editing, Methodology, Investigation, Conceptualization. **Mylène de Ruijter:** Writing – review & editing, Methodology, Investigation, Funding acquisition. **Miguel Castilho:** Writing – review & editing, Supervision, Resources, Methodology, Investigation, Funding acquisition, Conceptualization. **Jos Malda:** Writing – review & editing, Supervision, Resources, Project administration, Investigation, Funding acquisition, Conceptualization. **Rami K. Korhonen:** Writing – review & editing, Supervision, Resources, Project administration, Investigation, Funding acquisition, Conceptualization.

Declaration of competing interest

The authors declare that they have no known competing financial interests or personal relationships that could have appeared to influence the work reported in this paper.

Data availability

Data will be made available on request.

Acknowledgements

We would like thank Dr. Ervin Nippolainen for assisting with indentation testing, Mr. Tuomo Savolainen for manufacturing the Teflon molds, and Dr. Tak-Shing Fung for helpful guidance in statistical analyses.

Appendix A. Supplementary data

Supplementary data to this article can be found online at https://doi.org/10.1016/j.jmbbm.2023.105941.

References

Ateshian, G.A., 2009. The role of interstitial fluid pressurization in articular cartilage lubrication. J. Biomech. 42, 1163–1176. https://doi.org/10.1016/j.jbiomech.2009.04.040.

Ateshian, G.A., Rajan, V., Chahine, N.O., Canal, C.E., Hung, C.T., 2009. Modeling the matrix of articular cartilage using a continuous fiber angular distribution predicts many observed phenomena. J. Biomech. Eng. 131, 061003 https://doi.org/10.1115/1.3118773, 061003.

Bartnikowski, M., Wellard, R.M., Woodruff, M., Klein, T., 2015. Tailoring hydrogel viscoelasticity with physical and chemical crosslinking. Polymers 7, 2650–2669. https://doi.org/10.3390/polym7121539.

Bas, O., De-Juan-Pardo, E.M., Meinert, C., D'Angella, D., Baldwin, J.G., Bray, L.J., Wellard, R.M., Kollmannsberger, S., Rank, E., Werner, C., Klein, T.J., Catelas, I., Hutmacher, D.W., 2017. Biofabricated soft network composites for cartilage tissue engineering. Biofabrication 9, 025014. https://doi.org/10.1088/1758-5090/aa6b15.

Benya, P.D., Shaffer, J.D., 1982. Dedifferentiated chondrocytes reexpress the differentiated collagen phenotype when cultured in agarose gels. Cell 30, 215–224. https://doi.org/10.1016/0092-8674(82)90027-7.

Bertula, K., Martikainen, L., Munne, P., Hietala, S., Klefström, J., Ikkala, O., 2019. Nonappa, strain-stiffening of agarose gels. ACS Macro Lett. 8, 670–675. https://doi.org/10.1021/acsmacrolett.9b00258.

Bian, L., Fong, J.V., Lima, E.G., Stoker, A.M., Ateshian, G.A., Cook, J.L., Hung, C.T., 2010. Dynamic mechanical loading enhances functional properties of tissue-engineered cartilage using mature canine chondrocytes. Tissue Eng. 16, 1781–1790. https://doi.org/10.1089/ten.TEA.2009.0482.

Bian, L., Hou, C., Tous, E., Rai, R., Mauck, R.L., Burdick, J.A., 2013. The influence of hyaluronic acid hydrogel crosslinking density and macromolecular diffusivity on human MSC chondrogenesis and hypertrophy. Biomaterials 34, 413–421. https://doi.org/10.1016/j.biomaterials.2012.09.052.

Boere, K.W.M., Visser, J., Seyednejad, H., Rahimian, S., Gawlitta, D., van Steenbergen, M.J., Dhert, W.J.A., Hennink, W.E., Vermonden, T., Malda, J., 2014. Covalent attachment of a three-dimensionally printed thermoplast to a gelatin hydrogel for mechanically enhanced cartilage constructs. Acta Biomater. 10, 2602–2611. https://doi.org/10.1016/j.actbio.2014.02.041.

Bonnevie, E.D., Baro, V.J., Wang, L., Burris, D.L., 2012. Fluid load support during localized indentation of cartilage with a spherical probe. J. Biomech. 45, 1036–1041. https://doi.org/10.1016/j.jbiomech.2011.12.019.

Boontheekul, T., Kong, H.-J., Mooney, D.J., 2005. Controlling alginate gel degradation utilizing partial oxidation and bimodal molecular weight distribution. Biomaterials 26, 2455–2465. https://doi.org/10.1016/j.biomaterials.2004.06.044.

Bryant, S.J., Chowdhury, T.T., Lee, D.A., Bader, D.L., Anseth, K.S., 2004. Crosslinking density influences chondrocyte metabolism in dynamically loaded photocrosslinked poly(ethylene glycol) hydrogels. Ann. Biomed. Eng. 32, 407–417. https://doi.org/10.1023/B:ABME.0000017535.00602.ca.

Castilho, M., Hochleitner, G., Wilson, W., van Rietbergen, B., Dalton, P.D., Groll, J., Malda, J., Ito, K., 2018. Mechanical behavior of a soft hydrogel reinforced with three-dimensional printed microfibre scaffolds. Sci. Rep. 8, 1–10. https://doi.org/10.1038/s41598-018-19502-y.

Chahine, N.O., Wang, C.C.-B., Hung, C.T., Ateshian, G.A., 2004. Anisotropic strain-dependent material properties of bovine articular cartilage in the transitional range from tension to compression. J. Biomech. 37, 1251–1261. https://doi.org/10.1016/j.jbiomech.2003.12.008.

Chen, W.T., Engel, P.A., 1972. Impact and contact stress analysis in multilayer media. Int. J. Solid Struct. 8, 1257–1281. https://doi.org/10.1016/0020-7683(72)90079-0.

Chen, Y.-C., Lin, R.-Z., Qi, H., Yang, Y., Bae, H., Melero-Martin, J.M., Khademhosseini, A., 2012. Functional human vascular network generated in photocrosslinkable gelatin methacrylate hydrogels. Adv. Funct. Mater. 22, 2027–2039. https://doi.org/10.1002/adfm.201101662.

Cohen, B., Lai, W.M., Mow, V.C., 1998. A transversely isotropic biphasic model for unconfined compression of growth plate and chondroepiphysis. J. Biomech. Eng. 120, 491–496. https://doi.org/10.1115/1.2798019.

de Ruijter, M., Ribeiro, A., Dokter, I., Castilho, M., Malda, J., 2018. Simultaneous micropatterning of fibrous meshes and bioinks for the fabrication of living tissue constructs. Adv. Healthc. Mater., e1800418 https://doi.org/10.1002/adhm.201800418.

Ed-Daoui, A., Snabre, P., 2021. Poroviscoelasticity and compression-softening of agarose hydrogels. Rheol. Acta 60, 327–351. https://doi.org/10.1007/s00397-021-01267-3.

Elder, B.D., Athanasiou, K.A., 2009. Hydrostatic pressure in articular cartilage tissue engineering: from chondrocytes to tissue regeneration. Tissue Eng. B Rev. 15, 43–53. https://doi.org/10.1089/ten.teb.2008.0435.

Fung, Y.C., Tong, P., Chen, X., 2017. Classical and Computational Solid Mechanics, second ed. World Scientific Publishing Co Pte Ltd https://www.worldscientific.com/worldscibooks/10.1142/4134#t=aboutBook. (Accessed 31 December 2022).

Galarraga, J., Locke, R., Witherel, C., Stoeckl, B., Castilho, M., Mauck, R.L., Malda, J., Levato, R., Burdick, J.A., 2021. Fabrication of MSC-Laden Composites of Hyaluronic Acid Hydrogels Reinforced with MEW Scaffolds for Cartilage Repair. Biofabrication. https://doi.org/10.1088/1758-5090/ac3acb.

Gavénis, K., Kremer, A., Von Walter, M., Hollander, D.A., Schneider, U., Schmidt-Rohlfing, B., 2007. Effects of cyclic hydrostatic pressure on the metabolism of human osteoarthritic chondrocytes cultivated in a collagen gel. Artif. Organs 31, 91–98. https://doi.org/10.1111/j.1525-1594.2007.00347.x.

Gu, W.Y., Yao, H., Huang, C.Y., Cheung, H.S., 2003. New insight into deformation-dependent hydraulic permeability of gels and cartilage, and dynamic behavior of agarose gels in confined compression. J. Biomech. 36, 593–598. https://doi.org/10.1016/S0021-9290(02)00437-2.

Hashemnejad, S.M., Kundu, S., 2016. Strain stiffening and negative normal stress in alginate hydrogels. J. Polym. Sci., Part B: Polym. Phys. 54, 1767–1775. https://doi.org/10.1002/polb.24081.

Hayes, W.C., Keer, L.M., Herrmann, G., Mockros, L.F., 1972. A mathematical analysis for indentation tests of articular cartilage. J. Biomech. 5, 541–551. https://doi.org/10.1016/0021-9290(72)90010-3.

Hu, Y., Zhao, X., Vlassak, J.J., Suo, Z., 2010. Using indentation to characterize the poroelasticity of gels. Appl. Phys. Lett. 96, 121904 https://doi.org/10.1063/1.3370354.

Huang, A.H., Baker, B.M., Ateshian, G.A., Mauck, R.L., 2012. Sliding contact loading enhances the tensile properties of mesenchymal stem cell-seeded hydrogels. Eur. Cell. Mater. 24, 29–45. https://doi.org/10.22203/ecm.v024a03.

Kelly, T.-A.N., Roach, B.L., Weidner, Z.D., Mackenzie-Smith, C.R., O'Connell, G.D., Lima, E.G., Stoker, A.M., Cook, J.L., Ateshian, G.A., Hung, C.T., 2013. Tissue-engineered articular cartilage exhibits tension–compression nonlinearity reminiscent of the native cartilage. J. Biomech. 46, 1784–1791. https://doi.org/10.1016/j.jbiomech.2013.05.017.

Kock, L.M., Ito, K., van Donkelaar, C.C., 2013. Sliding indentation enhances collagen content and depth-dependent matrix distribution in tissue-engineered cartilage constructs. Tissue Eng. 19, 1949–1959. https://doi.org/10.1089/ten.tea.2012.0688.

Lee, K.Y., Mooney, D.J., 2012. Alginate: properties and biomedical applications. Prog. Polym. Sci. 37, 106–126. https://doi.org/10.1016/j.progpolymsci.2011.06.003.

Luo, Z.-J., Seedhom, B.B., 2007. Light and low-frequency pulsatile hydrostatic pressure enhances extracellular matrix formation by bone marrow mesenchymal cells: an in-vitro study with special reference to cartilage repair. Proc. Inst. Mech. Eng. [H]. 221, 499–507. https://doi.org/10.1243/09544119JEIM199.

Maas, S.A., Ellis, B.J., Ateshian, G.A., Weiss, J.A., 2012. FEBio: finite elements for biomechanics. J. Biomech. Eng. 134, 011005 https://doi.org/10.1115/1.4005694.

Mak, A.F., 1986. The apparent viscoelastic behavior of articular cartilage—the contributions from the intrinsic matrix viscoelasticity and interstitial fluid flows. J. Biomech. Eng. 108, 123–130. https://doi.org/10.1115/1.3138591.

Markert, C.D., Guo, X., Skardal, A., Wang, Z., Bharadwaj, S., Zhang, Y., Bonin, K., Guthold, M., 2013. Characterizing the micro-scale elastic modulus of hydrogels for use in regenerative medicine. J. Mech. Behav. Biomed. Mater. 27, 115–127. https://doi.org/10.1016/j.jmbbm.2013.07.008.

Mauck, R.L., Soltz, M.A., Wang, C.C.B., Wong, D.D., Chao, P.-H.G., Valhmu, W.B., Hung, C.T., Ateshian, G.A., 2000. Functional tissue engineering of articular cartilage through dynamic loading of chondrocyte-seeded agarose gels. J. Biomech. Eng. 122, 252–260. https://doi.org/10.1115/1.429656.

Meloni, G.R., Fisher, M.B., Stoeckl, B.D., Dodge, G.R., Mauck, R.L., 2017. Biphasic finite element modeling reconciles mechanical properties of tissue-engineered cartilage constructs across testing platforms. Tissue Eng. 23, 663–674. https://doi.org/10.1089/ten.tea.2016.0191.

Miri, A.K., Hosseinabadi, H.G., Cecen, B., Hassan, S., Zhang, Y.S., 2018. Permeability mapping of gelatin methacryloyl hydrogels. Acta Biomater. 77, 38–47. https://doi.org/10.1016/j.actbio.2018.07.006.

Miyanishi, K., Trindade, M.C.D., Lindsey, D.P., Beaupré, G.S., Carter, D.R., Goodman, S. B., Schurman, D.J., Smith, R.L., 2006. Dose- and time-dependent effects of cyclic hydrostatic pressure on transforming growth factor-β3-induced chondrogenesis by adult human mesenchymal stem cells in vitro. Tissue Eng. 12, 2253–2262. https://doi.org/10.1089/ten.2006.12.2253.

Moo, E.K., Tanska, P., Federico, S., Al-Saffar, Y., Herzog, W., Korhonen, R.K., 2021. Collagen fibres determine the crack morphology in articular cartilage. Acta Biomater. 126, 301–314. https://doi.org/10.1016/j.actbio.2021.03.031.

Moo, E.K., Ebrahimi, M., Sibole, S.C., Tanska, P., Korhonen, R.K., 2022. The intrinsic quality of proteoglycans, but not collagen fibres, degrades in osteoarthritic cartilage. Acta Biomater. https://doi.org/10.1016/j.actbio.2022.09.002.

Moore, A.C., Zimmerman, B.K., Chen, X., Lu, X.L., Burris, D.L., 2015. Experimental characterization of biphasic materials using rate-controlled Hertzian indentation. Tribol. Int. 89, 2–8. https://doi.org/10.1016/j.triboint.2015.02.001.

Mullins, L., 1947. Effect of stretching on the properties of rubber. J. Rubber Res. 16, 275–289. https://doi.org/10.5254/1.3546914.

Nam, S., Hu, K.H., Butte, M.J., Chaudhuri, O., 2016. Strain-enhanced stress relaxation impacts nonlinear elasticity in collagen gels. Proc. Natl. Acad. Sci. USA 113, 5492–5497. https://doi.org/10.1073/pnas.1523906113.

Nia, H.T., Han, L., Li, Y., Ortiz, C., Grodzinsky, A., 2011. Poroelasticity of cartilage at the nanoscale. Biophys. J. 101, 2304–2313. https://doi.org/10.1016/j.bpj.2011.09.011.

Ogden, R.W., Roxburgh, D.G., 1999. A pseudo–elastic model for the Mullins effect in filled rubber. Proc. R. Soc. Lond. Ser. Math. Phys. Eng. Sci. 455, 2861–2877. https://doi.org/10.1098/rspa.1999.0431.

Peiffer, Q.C., de Ruijter, M., van Duijn, J., Crottet, D., Dominic, E., Malda, J., Castilho, M., 2020. Melt electrowriting onto anatomically relevant biodegradable substrates: resurfacing a diarthrodial joint. Mater. Des. 195, 109025 https://doi.org/10.1016/j.matdes.2020.109025.

Pernodet, N., Maaloum, M., Tinland, B., 1997. Pore size of agarose gels by atomic force microscopy. Electrophoresis 18, 55–58. https://doi.org/10.1002/elps.1150180111.

Rees, D.A., Welsh, E.J., 1977. Secondary and tertiary structure of polysaccharides in solutions and gels. Angew. Chem., Int. Ed. Engl. 16, 214–224. https://doi.org/10.1002/anie.197702141.

Roach, B.L., Nover, A.B., Ateshian, G.A., Hung, C.T., 2016. Agarose hydrogel characterization for regenerative medicine applications: focus on engineering cartilage. In: Biomater. Nat. Adv. Devices Ther. John Wiley & Sons, Ltd, pp. 258–273. https://doi.org/10.1002/9781119126218.ch16.

Schuurman, W., Levett, P.A., Pot, M.W., van Weeren, P.R., Dhert, W.J.A., Hutmacher, D. W., Melchels, F.P.W., Klein, T.J., Malda, J., 2013. Gelatin-Methacrylamide hydrogels as potential biomaterials for fabrication of tissue-engineered cartilage constructs. Macromol. Biosci. 13, 551–561. https://doi.org/10.1002/mabi.201200471.

Soltz, M.A., Stankiewicz, A., Ateshian, G., Mauck, R.L., Hung, C.T., 1999. Direct Hydraulic Permeability Measurements of Agarose Hydrogels Used as Cell Scaffolds. American Society of Mechanical Engineers Digital Collection, pp. 229–230. https://doi.org/10.1115/IMECE1999-0461.

Stevanovic, M., Yovanovich, M.M., Culham, J.R., 2000. Modeling contact between rigid sphere and elastic layer bonded to rigid substrate. In: ITHERM 2000 Seventh Intersoc. Conf. Therm. Thermomechanical Phenom. Electron. Syst. Cat No00CH37069, pp. 29–35. https://doi.org/10.1109/ITHERM.2000.866804.

Townsend, J., Koep, N., Weichwald, S., 2016. Pymanopt: a Python toolbox for optimization on manifolds using automatic differentiation. J. Mach. Learn. Res. 17, 1–5.

Van Den Bulcke, A.I., Bogdanov, B., De Rooze, N., Schacht, E.H., Cornelissen, M., Berghmans, H., 2000. Structural and rheological properties of methacrylamide modified gelatin hydrogels. Biomacromolecules 1, 31–38. https://doi.org/10.1021/bm990017d.

Virtanen, P., Gommers, R., Oliphant, T.E., Haberland, M., Reddy, T., Cournapeau, D., Burovski, E., Peterson, P., Weckesser, W., Bright, J., van der Walt, S.J., Brett, M., Wilson, J., Millman, K.J., Mayorov, N., Nelson, A.R.J., Jones, E., Kern, R., Larson, E., Carey, C.J., Polat, İ., Feng, Y., Moore, E.W., VanderPlas, J., Laxalde, D., Perktold, J., Cimrman, R., Henriksen, I., Quintero, E.A., Harris, C.R., Archibald, A.M., Ribeiro, A. H., Pedregosa, F., van Mulbregt, P., 2020. SciPy 1.0: fundamental algorithms for scientific computing in Python. Nat. Methods 17, 261–272. https://doi.org/10.1038/s41592-019-0686-2.

Visser, J., Melchels, F.P.W., Jeon, J.E., van Bussel, E.M., Kimpton, L.S., Byrne, H.M., Dhert, W.J.A., Dalton, P.D., Hutmacher, D.W., Malda, J., 2015. Reinforcement of hydrogels using three-dimensionally printed microfibres. Nat. Commun. 6, 6933. https://doi.org/10.1038/ncomms7933.

Wahlquist, J.A., DelRio, F.W., Randolph, M.A., Aziz, A.H., Heveran, C.M., Bryant, S.J., Neu, C.P., Ferguson, V.L., 2017. Indentation mapping revealed poroelastic, but not viscoelastic, properties spanning native zonal articular cartilage. Acta Biomater. 64, 41–49. https://doi.org/10.1016/j.actbio.2017.10.003.

Yue, K., Trujillo-de Santiago, G., Alvarez, M.M., Tamayol, A., Annabi, N., Khademhosseini, A., 2015. Synthesis, properties, and biomedical applications of gelatin methacryloyl (GelMA) hydrogels. Biomaterials 73, 254–271. https://doi.org/10.1016/j.biomaterials.2015.08.045.